层状岩体晶粥中压实作用效率

——来自扬子地块北缘望江山岩体中部带矿物晶体粒度分布(CSDs)和空间展布形式(SDPs)的约束

李中州,王梦玺,张步乾,王洁

长安大学地球科学与资源学院,西安,710054

内容提要:层状岩体冷凝中—晚期有铁钛氧化物结晶时,晶粥中粒间熔体的排出方式常以压实作用为主,但不同层位压实作用的效率往往不同,目前对控制压实作用效率的主要机制尚不清楚。笔者等以扬子北缘出露规模较大、分异程度较高的新元古代望江山层状岩体作为研究对象,利用斜长石、单斜辉石的晶体粒度分布(CSDs)和空间展布形式(SDPs)分析,探讨了岩体中部带下段(MZa)橄榄辉长苏长岩、辉长苏长岩和中部带上段(MZb)氧化物辉长岩粒间熔体的排出机制及其效率。岩体 MZa 和 MZb 中斜长石和单斜辉石的 CSD 曲线均具有相互平行的特征,SDP 图解具有负相关趋势,分别与机械压实的特征和趋势一致,表明各岩相带粒间熔体的排出方式均为机械压实。模拟计算得到橄榄辉长苏长岩、辉长苏长岩和氧化物辉长岩中封闭粒间熔体比例(F_{TL})分别为:28%～33%,14%～23%和7%～12%,表明从 MZa 到 MZb 机械压实逐渐增强。MZa 中橄榄辉长苏长岩斜长石 CSD 截距最大(2.23～3.78),特征长最小(0.29～0.45)且小颗粒斜长石具有较大长宽比(5∶1～11∶1),表明岩浆冷却速率较快,导致压实效率最低,粒间熔体未被有效排出。MZa 中辉长苏长岩斜长石 CSD 截距减小(1.31～2.60),特征长增大(0.43～0.58)且小颗粒斜长石长宽比减小(<5∶1),说明冷却速率变慢,导致压实效率提高,粒间熔体被有效排出。MZb 氧化物辉长岩中斜长石 CSD 截距进一步减小(0.49～1.60),特征长进一步增大(0.53～0.69)且小颗粒斜长石具有低长宽比(<5∶1),说明冷却速率进一步降低,同时相较于橄榄辉长苏长岩和辉长苏长岩堆晶矿物与粒间熔体密度差增大,压实效率进一步提高,粒间熔体排出程度达到最高。因此,层状岩体晶粥中机械压实效率主要受控于堆晶矿物与粒间熔体密度差以及岩浆冷却速率,当冷却速率较低并有大量铁钛氧化物结晶时机械压实作用的效率最高。

关键词:压实作用;粒间熔体排出机制;晶体粒度分布;空间展布形式;望江山层状岩体;扬子地块北缘

根据镁铁—超镁铁质层状岩体原位结晶模型,岩浆房从边部到中部由致密堆晶岩、晶粥和主体岩浆组成(Campbell, 1978; Kuritani et al., 2007; Namur et al., 2014),其中致密堆晶岩全部由结晶矿物组成,不含熔体,而主体岩浆全部由熔体组成,不含结晶矿物,晶粥介于前两者之间,由堆晶矿物和粒间熔体共同组成(Wager et al., 1960)。前人研究认为晶粥中初始粒间熔体比例高达 50%～70%(Campbell, 1978; Shirley, 1986; Philpotts et al., 1998; Jerram et al., 2003, Donev et al., 2004),但冷凝成岩后其比例降至 7%～60%(Irvine, 1982; Namur and Humphreys, 2018),相应的堆晶岩在矿物组成、结构构造和化学成分上也存在较大差异(Irvine, 1982; Tegner et al., 2009; Namur and Charlier, 2012),表明晶粥中粒间熔体的排出与层状岩体冷凝时的一系列物理过程有关。因此,对粒间熔体排出机制的研究有助于理解层状岩体的岩浆演化过程(Boorman et al., 2004; Holness et al., 2007, 2017; Tegner et al., 2009; Cashman et al., 2017; Yao Zhuosen et al., 2021; Wang Mengxi et al., 2022)。

粒间熔体从晶粥中排出的机制主要有成分对流(Compositional convection; Tait et al., 1984; Toplis et al., 2008)和压实作用(Compaction; Tegner et al., 2009; McKenzie, 1984, 2011)。成分对流作用发生的前提是粒间熔体和主体岩浆之间存在较大密

注:本文为国家自然科学基金资助项目(编号:41972057)、陕西省自然科学基础研究计划一般项目(面上)(编号:2018JM4009)和中央高校基本科研业务费(编号:300102271208)的成果。

收稿日期:2022-01-31;改回日期:2022-06-09;网络首发:2022-06-20;责任编辑:刘志强。Doi: 10.16509/j.georeview.2022.06.161

作者简介:李中州,男,1996 年生,硕士研究生,矿物学、岩石学、矿床学方向;Email: zhongzhouli@yeah.net。通讯作者:王梦玺,男,1986 年生,博士,副教授,主要从事岩浆作用与成矿研究;Email: mxwang@chd.edu.cn。

度差(Tait et al., 1984; Sparks and Huppert, 1984; Tait and Jaupart, 1992; Toplis et al., 2008),当晶粥中熔体密度低于上覆主体岩浆时会形成密度的不稳定分布导致粒间熔体与主体岩浆的交换(Namur and Charlier, 2012)。压实作用主要发生在粒间熔体和堆晶矿物存在较大密度差的情况下(McKenzie, 1984, 2011; Tegner et al., 2009; Namur and Charlier, 2012; Holness et al., 2017),在粒间熔体排出过程中可能更加普遍(Holness et al., 2017)。根据堆晶岩中矿物是否发生黏性变形,可将压实作用分为机械压实(Mechanical compaction)和变形压实(Deformational compaction)。机械压实仅使矿物发生紧密堆积从而将粒间熔体排出,矿物并未产生变形,也不会形成明显的岩浆面理(Higgins, 1991)。而当压实程度大于 50%时,会引起晶体形态的变化发生变形压实(Hunter, 1996; Meurer and Boudreau, 1998),并产生明显的岩浆面理。当粒间熔体的比例较少、压实程度更高时,将发生压溶作用,表现为垂直于应力方向的矿物溶解—重结晶(Rutter, 1983; Hunter, 1996; Meurer and Boudreau, 1998; Holness et al., 2017)。不同类型的压实作用效率不同,即使同一种压实作用,在不同岩体以及同一岩体不同岩相带中效率也不尽相同。前人研究表明,压实效率与压实速率和堆晶速率的相对大小、堆晶矿物和粒间熔体的密度差以及岩浆的冷却速率等因素有关(Tegner et al., 2009; Namur and Charlier, 2012),然而这些因素之间的相互关系及其如何控制压实效率的变化尚不清楚。

前人研究表明层状岩体中矿物晶体粒度分布(Crystal size distributions, CSDs)和空间展布形式(Spatial distribution patterns, SDPs)可以有效指示岩浆房中的一系列物理过程(Jerram et al., 1996, 2003; Higgins, 2002a; Boorman et al., 2004; Kaufmann et al., 2019; Wang Mengxi and Wang Christina Yan, 2020)。晶体粒度分布曲线以晶体粒度为横坐标,布居密度(单位体积内晶体数)的自然对数为纵坐标(Marsh, 1988)。层状岩体岩浆房中不同的物理过程具有不同的 CSD 曲线,通过 CSD 曲线及其斜率、截距等参数特征可以识别岩浆房中的动力学过程,如晶体成核与生长速率的变化、结构粗化、压实作用和成分对流等(Marsh, 1988; Boorman et al., 2004; Higgins, 2002a; 2006a)。机械压实由于粒间熔体被排出后矿物颗粒之间距离减小而布居密度增大,使初始平直的 CSD 曲线发生平行上移,表现为一系列相互平行的 CSD 曲线(Higgins, 2002a)。变形压实中压溶作用 CSD 曲线不仅表现为向上平移,而且小颗粒处斜率变缓(Higgins, 2002a)。成分对流常表现为粒间熔体和上覆主体岩浆之间的成分交换(Tait et al., 1984; Toplis et al., 2008),会使粒度大小不同的晶体混合而产生类似岩浆混合的下凹型 CSD 曲线(Higgins, 1996; Higgins and Roberge, 2007)。晶体空间展布形式(SDPs)常通过样品中目标矿物之外的所有其他矿物含量之和与 R 值(矿物所有颗粒间最短相邻距离的观测值和预测值之比)的相关关系来表示,可以用来识别岩体冷凝过程中机械压实、变形压实、过度生长和分选增强等过程(Jerram et al., 1996, 2003)。因此,层状岩体中矿物的 CSDs 和 SDPs 相结合可以用来探讨晶粥中粒间熔体的排出机制。

望江山岩体是扬子北缘新元古代汉南杂岩带中规模较大的层状岩体(李行等,1995;Zhou Meifu et al., 2002; 凌文黎等,2001;苏犁,2004),出露面积约 100 km^2,与全球典型的 Skaergaard 层状岩体规模相当(Nielsen, 2004)。望江山岩体由下部带、中部带和上部带组成,其中下部带主要由纯橄岩、橄长岩和辉石岩组成,中部带由橄榄辉长苏长岩、橄榄辉长岩、辉长岩和辉长苏长岩组成,上部带主要为辉长闪长岩(苏犁,2004)。岩体中部带厚度较大(约 2000 m),构成该岩体的主体,从底部到顶部斜长石和单斜辉石具有不同的晶体粒度、长宽比和定向程度等特征,不同岩相带在岩石结构和矿物组成方面也表现出较大差异,尤其是不同岩相带铁钛氧化物含量的差异,说明望江山岩体中部带不同岩石类型具有不同的岩浆演化过程,是研究浅部岩浆房粒间熔体排出机制及岩浆演化的理想对象。因此,本文对望江山岩体中部带不同岩相带的斜长石和单斜辉石进行了 CSDs 和 SDPs 分析,探讨望江山岩体中部带冷凝过程中粒间熔体的排出机制及其效率,同时也对阐明层状岩体晶粥的冷凝过程和粒间熔体演化具有一定意义。

1 地质背景

华南板块由扬子地块和华夏地块在中—新元古代拼合而成(图 1a)(Chen Jiangfeng et al., 1991; Zhao Guochun et al., 2012)。扬子地块北缘以秦岭—大别—苏鲁造山带为界和华北板块南缘相接,西缘以松潘—甘孜造山带为界和青藏高原东部相接(图 1a)。扬子地块由基底杂岩和上覆震旦系—中

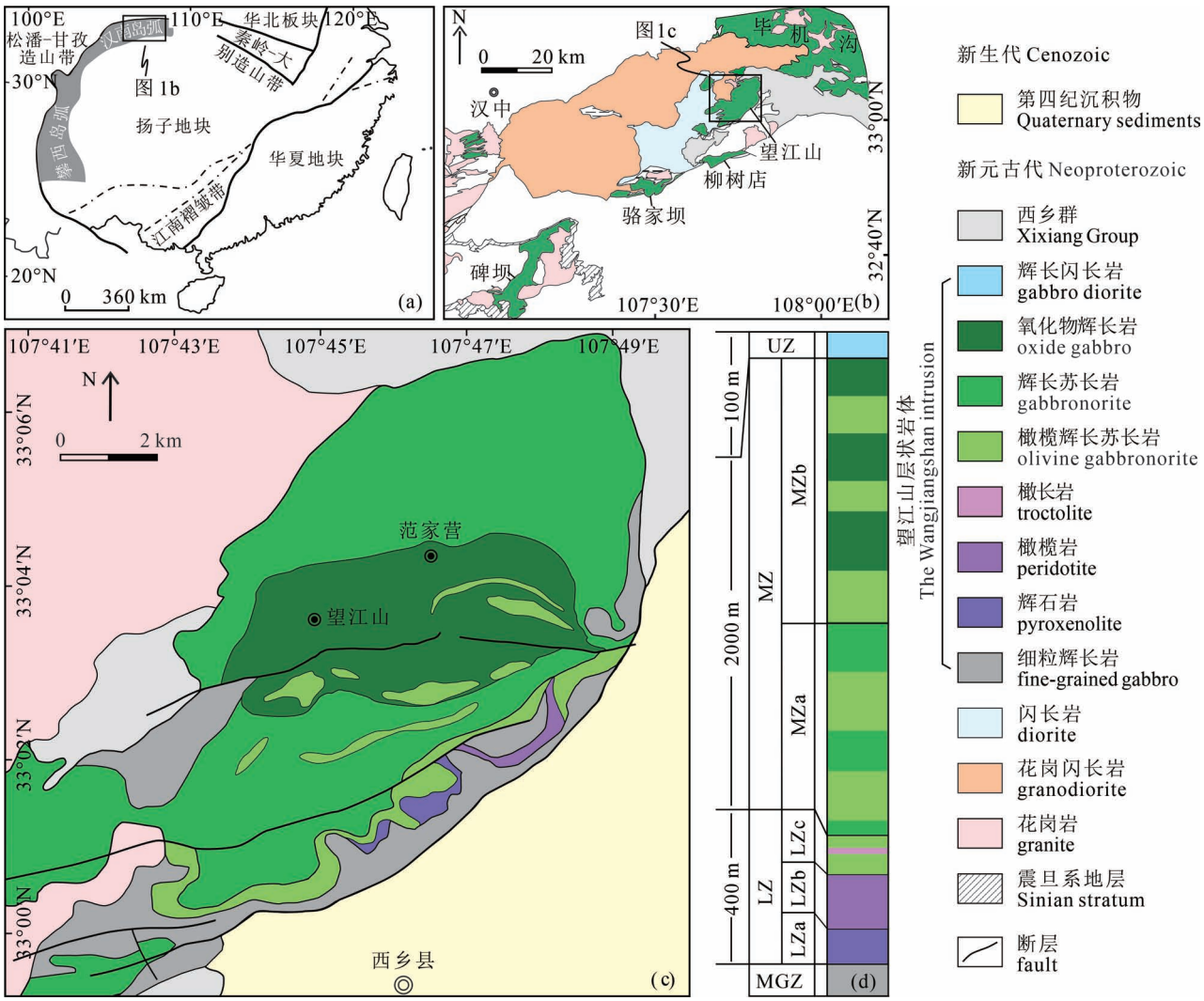

图 1（a）扬子地块北缘和西缘新元古代汉南—攀西岛弧地质图(据 Zhao Guochun and Cawood, 2012 修改);(b) 扬子地块北缘新元古代汉南杂岩带中镁铁—超镁铁质岩体分布图(据 Wang Mengxi and Wang Christina Yan, 2020 修改);(c) 望江山岩体地质简图(据李行等,1995 修改);(d) 望江山岩体综合岩相柱状图(据李行等,1995;苏犁,2004 修改)

Fig. 1 (a) Schematic geological map showing Neoproterozoic Hannan—Panxi island arc in the northern and western margins of the Yangtze Block (modified after Zhao and Cawood, 2012); (b) simplified geological map showing Neoproterozoic mafic—ultramafic intrusions in the Hannan arc in the northern margin of the Yangtze Block (modified after Wang Mengxi and Wang Christina Yan, 2020); (c) plan view of the Wangjiangshan layered intrusion (modified after Li Hang et al., 1995&); (d) an integrated stratigraphic column of the Wangjiangshan intrusion (modified after Li Hang et al., 1995&; Su Li, 2004&)

生界盖层组成,基底主要由太古宇角闪岩、中元古界变质沉积岩、新元古界地层和大量侵入岩组成(高山等,1990;Gao Shan et al., 1999; 凌文黎等,2006;赵凤清等,2006;徐学义等,2009;王梦玺等,2012;刘伟等,2018;旷红伟,2019;高峰,2020),盖层主要为上震旦统—上侏罗统的碎屑岩、碳酸盐岩、变火山岩和一些冰川沉积物(Yan Danping et al., 2003)。

扬子地块北缘新元古代汉南杂岩带中发育有大量呈北东—南西向展布的镁铁—超镁铁质岩体(图 1b),这些岩体侵位于中—新元古代火地垭群和西乡群,并被震旦系地层不整合覆盖(凌文黎等,2001,2006;徐学义等,2009,2010;李婷,2010;敖文昊等,2014;耿元生等,2017)。汉南杂岩带中镁铁—超镁铁质岩体主要包括~870 Ma 碑坝、~825 Ma 望江山、~785 Ma 毕机沟和~746 Ma 骆家坝岩体(Zhou Meifu et al., 2002; Zhao Junhong and Zhou Meifu, 2009; Wang Mengxi et al., 2016)。毕机沟岩体是汉南杂岩带中出露规模最大的层状岩体,面积

约 500 km^2,自下而上可划分为 3 个岩相带,下部带主要由橄榄岩和辉石岩组成,中部带由辉长岩组成,上部带主要由石英辉长岩组成(Zhou Meifu et al., 2002)。碑坝岩体出露面积约 150 km^2,岩性分异较好,从下到上主要由橄榄辉长岩、辉长岩和闪长岩组成(Zhao Junhong and Zhou Meifu, 2009)。骆家坝岩体为中细粒角闪辉长岩组成的小型镁铁质岩体(Zhao Junhong and Zhou Meifu, 2009)。

望江山岩体是汉南杂岩带中出露规模仅次于毕机沟的第二大层状岩体,长约 17 km、宽约 7 km,侵位于新元古代西乡群(图 1c)(李行等,1995;凌文黎等,2001;Zhao Junhong and Zhou Meifu, 2009)。根据矿物组合的变化,前人将望江山岩体从下到上依次划分为:基底带(MGZ)、下部超镁铁岩带(LZ)、中部辉长岩带(MZ)、上部辉长闪长岩带(UZ)(图 1d)(苏犁, 2004)。基底带为一套细粒辉长岩,普遍出现西乡群基性火山岩和碎屑岩的角砾和团块。下部带厚度约 300~400 m,从下到上可分为 3 段:下段(LZa)主要由辉石岩和橄榄辉石岩组成,中段(LZb)主要由含长橄榄岩、橄榄岩组成,上段(LZc)主要由橄榄辉长苏长岩组成,其中橄榄辉石岩和橄长岩中赋存有厚度不一的铜镍(铂)矿化层。中部带为望江山岩体的主体,总厚度近 2000 m,主要由橄榄辉长苏长岩、橄榄辉长岩、苏长辉长岩、氧化物辉长岩组成,根据岩性变化可将其划分为五个韵律层,各韵律层从底部到顶部岩性由细粒橄榄辉长苏长岩、细粒橄榄辉长岩渐变为中—粗粒辉长苏长岩或中—粗粒氧化物辉长岩(李行等,1995;苏犁,2004)。上部带主要由辉长闪长岩和含石英闪长岩组成,含少量角闪辉长岩,厚度约 100 m,具有较清晰的韵律层状构造,与下伏中—粗粒氧化物辉长岩呈渐变过渡关系。

根据钒钛磁铁矿含矿性的不同将望江山岩体中部带从下到上依次划分为:①不含矿辉长苏长岩相带(MZa),主要由两个从底部橄榄辉长苏长岩或橄榄辉长岩向上渐变为辉长苏长岩的韵律层组成;②含矿氧化物辉长岩相带(MZb),主要由 3 个从底部橄榄辉长岩向上渐变为氧化物辉长岩的韵律层组成(图 1d)。本研究在岩体中心相不同岩相带进行了系统采样,选取 MZa 中第二韵律层的 3 个橄榄辉长苏长岩样品、4 个辉长苏长岩样品和 MZb 中第一韵律层的 5 个氧化物辉长岩样品进行 CSDs 和 SDPs 分析。

2 岩相学特征

2.1 橄榄辉长苏长岩

橄榄辉长苏长岩具有中堆晶结构(图 2a),主要由堆晶相斜长石(45%~50%)、斜方辉石(10%~15%)和橄榄石(3%~10%)、粒间相普通角闪石(10%~15%)、黑云母(1%~3%)、钛铁矿(1%~2%)、磁铁矿(<1%)以及同时呈堆晶相和粒间相产出的单斜辉石(15%~20%)组成。橄榄石(0.1~1.0 mm)呈粒状,常包含在结晶较晚的斜长石、辉石和角闪石中形成包橄结构。斜长石(0.1~2.0 mm,最大 2.7×0.7 mm)呈自形—半自形长柱状,长宽比一般为 2∶1 到 6∶1,最大可达 11∶1,环带结构发育(图 2a),主要为具有核($An_{63~68}$)—边($An_{39~56}$)结构的正环带(王岩, 2019)。斜方辉石(0.1~1.5 mm)和少数单斜辉石(0.1~1.5 mm)呈自形—半自形短柱状,发育有角闪石反应边,局部单斜辉石中包裹斜长石。粒间相单斜辉石(0.2~2.0 mm)、角闪石(0.2~2.0 mm)、黑云母(0.2~1.5 mm)和铁钛氧化物(0.1~1.0 mm)呈不规则他形粒状,充填于堆晶矿物之间,其晶体形态主要受堆晶矿物间隙形状影响,局部较大的普通角闪石或单斜辉石将堆晶相斜长石或橄榄石完全包裹。

2.2 辉长苏长岩

辉长苏长岩为补堆晶结构(图 2b),主要由堆晶相斜长石(55%~65%)和斜方辉石(15%~20%),粒间相普通角闪石(1%~5%)、钛铁矿(2%~4%)、磁铁矿(1%~2%)和磷灰石(1%~5%)组成,单斜辉石同时以堆晶相和粒间相产出(20%~25%)。斜长石呈自形—半自形长柱状,粒度以 0.2~2.0 mm 为主,粒度最大可达 1.0×6.0 mm,长宽比为 2∶1 到 4∶1,少数最大可达 8∶1,低于橄榄辉长苏长岩中相应比值,环带结构较发育(图 2b),主要为核($An_{65~71}$)—边($An_{55~57}$)结构的正环带和核($An_{54~59}$)—边($An_{60~72}$)结构的反环带(王岩, 2019),个别样品斜长石显示定向排列(图 2b),局部偶见弯曲变形,显示不一致消光。斜方辉石(0.2~1.5 mm)和单斜辉石(0.2~1.5 mm)呈自形—半自形短柱状,发育有角闪石反应边结构,局部单斜辉石包含有自形斜长石。粒间相铁钛氧化物(0.1~1.0 mm)、普通角闪石(0.2~2.0 mm)、磷灰石(0.1~0.5 mm)和单斜辉石(0.2~2.0 mm)呈他形粒状充填于堆晶矿物之间,含量低于橄榄辉长苏长岩中粒间相矿物。

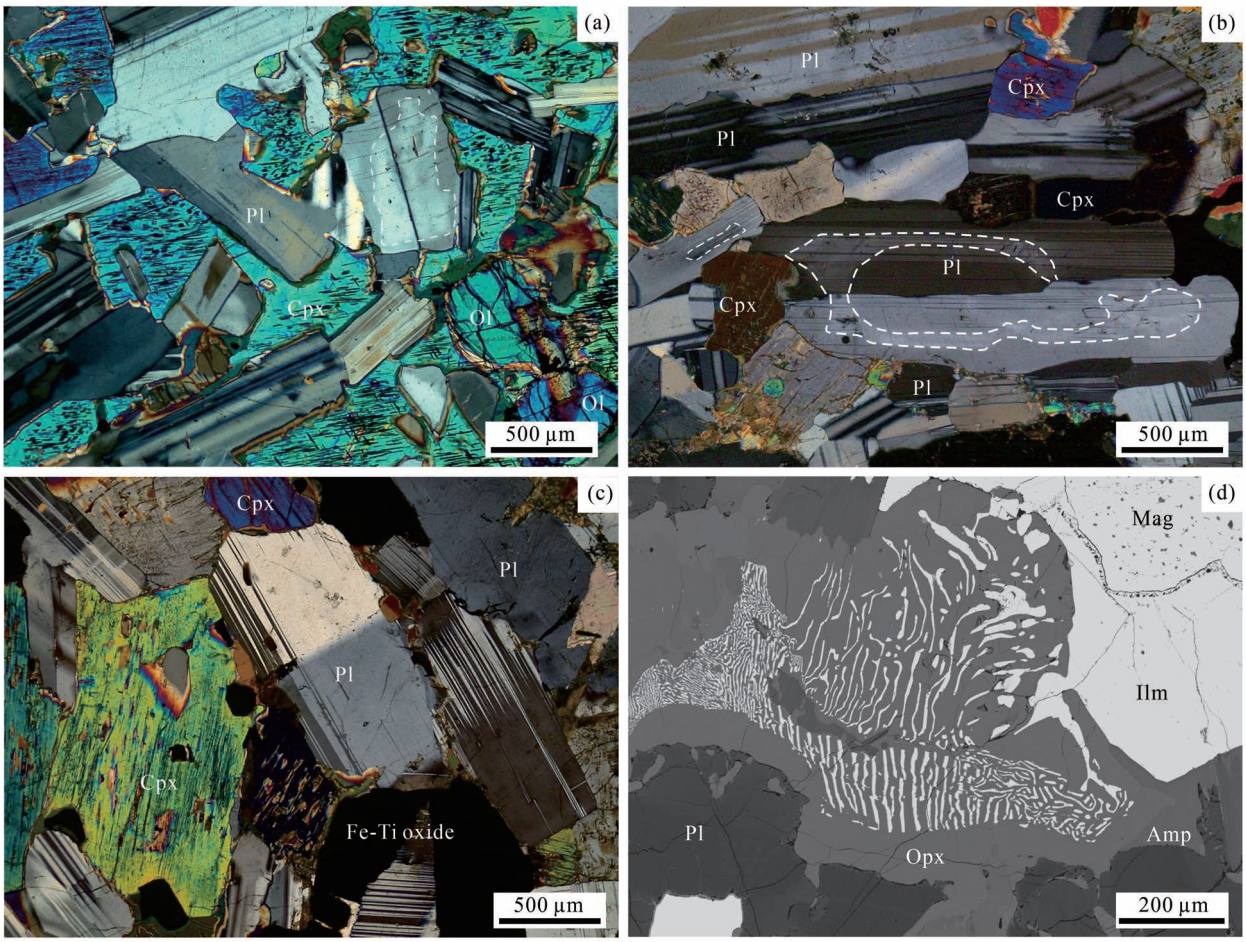

图 2 扬子地块北缘望江山岩体中部带不同岩石类型岩相学特征

Fig. 2 Photomicrographs of samples from the MZ of the Wangjiangshan intrusion in the northern margin of the Yangtze Block

(a) 橄榄辉长苏长岩中自形斜长石为堆晶相矿物,并发育有环带结构,单斜辉石自形程度较差,作为粒间相填充于斜长石颗粒之间,正交偏光,样品 WJS-21;(b) 辉长苏长岩中斜长石为主要堆晶相,具有较弱的定向排列,环带结构发育,他形单斜辉石为粒间相矿物,正交偏光,样品 WJS-30;(c) 氧化物辉长岩中斜长石和单斜辉石为堆晶矿物,其中偶见斜长石显示不一致消光,他形铁钛氧化物为粒间相矿物,正交偏光,样品 WJS-24;(d) 氧化物辉长岩中蠕虫状的钛铁矿与辉石构成替代交生体,背散射图像,样品 WJS-24(Pl—斜长石;Cpx—单斜辉石;Opx—斜方辉石;Ol—橄榄石;Fe—Ti oxide—铁钛氧化物 ;Ilm—钛铁矿;Mag—磁铁矿)

(a) Cumulus plagioclase (Pl) laths are euhedral in shape with compositional zoning, and anhedral clinopyroxene (Cpx) grains occur as interstitial phase to cumulus plagioclase (Pl) in olivine gabbronorite. Cross-polarizer and transmitted light, sample WJS-21; (b) Cumulus plagioclase (Pl) grains show a weak alignment with compositional zoning, and clinopyroxene (Cpx) grains occur as interstitial phase in gabbronorite. Cross-polarizer and transmitted light, sample WJS-30; (c) Plagioclase (Pl) grains with undulose extinction occur as cumulus, with interstitial Fe—Ti oxides in oxide gabbro. Cross-polarizer and transmitted light, sample WJS-24; (d) The replacive symplectites are composed of orthopyroxene (Opx) and vermicule ilmenite (Ilm) in oxide gabbro. BSE image, sample WJS-24

2.3　氧化物辉长岩

氧化物辉长岩为补堆晶结构(图 2c),主要由堆晶相斜长石(50%~65%)和斜方辉石(5%~10%),粒间相普通角闪石(5%~10%)、磁铁矿(8%~10%)、钛铁矿(2%~5%)以及同时以堆晶相和粒间相产出的单斜辉石(20%~25%)组成。斜长石呈自形—半自形长柱状,粒度以 0.2~4.0 mm 为主,最大可达 1.0×7.5 mm,长宽比集中于 2∶1 到 6∶1,少数可达 11∶1,斜长石成分均一($An_{54\sim58}$),环带结构不发育(王岩,2019),局部偶见定向排列和弯曲变形,并显示不一致消光,面理不发育(图 2c)。斜方辉石(0.2~2.0 mm)和单斜辉石(0.2~2.0 mm)呈自形—半自形短柱状,内部发育有出溶的针状铁钛氧化物,个别发育有角闪石反应边(图 2c)。铁钛氧化物(0.1~1.5 mm)呈自形—半自形粒状,小颗粒晶体常被粒间相单斜辉石包裹。粒间相单斜辉石

(0.2~1.5 mm)、普通角闪石(0.2~2.0 mm)、磁铁矿和钛铁矿(0.2~1.0 mm)以他形粒状充填于堆晶矿物颗粒之间,其中铁钛氧化物将斜长石、辉石熔蚀为港湾状或浑圆状;局部出现由斜方辉石和磁铁矿组成的替代交生体(图 2d),其中辉石体积约占 60%~70%,蠕虫状磁铁矿约占 30%~40%,宽度一般为 1~50 μm。替代交生体根矿物为不规则粒状铁钛氧化物,被替代矿物为斜长石。

3 分析方法

由于望江山岩体中部带在野外露头并未出现明显的岩浆流面和流线,岩相观察也未见明显的矿物定向排列,因此我们对该带 12 个新鲜岩石样品磨制常规薄片时切片方向为随机选取。利用超景深光学显微镜拍摄薄片不同位置的单偏光和正交偏光显微照片,然后通过电脑自动拼接得到整个薄片的照片。在绘图软件中对所得照片进行矿物颗粒轮廓的描绘,为了准确识别矿物边界,需要对显微照片中相互接触的同种矿物颗粒边界在显微镜下旋转载物台进行区分,保证每个颗粒的边界都是准确的。本次研究能够识别的最小矿物颗粒为 0.03 mm。

将得到的斜长石和单斜辉石灰度图利用 ImageJ 软件分别进行分析,统计颗粒的大小、圆度和长宽比等参数。晶体三维形态用三轴比,即短轴:中轴:长轴(S:I:L)表示,晶体实际的 S/I 值一般为薄片中晶体切面长/宽比(L/W)的众数(Higgins, 1994),I/L 值一般采用薄片中晶体切面长/宽(L/W)的偏度统计值进行估算(Higgins, 1994; Garrido et al., 2001)。而对于自形程度较高的斜长石和单斜辉石,最准确的三轴比应当保证颗粒在二维薄片中的含量和利用 CSDs 计算出的三维体积含量非常接近(Higgins, 2002a, b)。本次研究样品中,斜长石、单斜辉石均呈自形—半自形,通过对比薄片中矿物含量与 CSD 的体积含量,确定斜长石三轴比(S:I:L)为 1:2.7:3.0,单斜辉石三轴比(S:I:L)为 1:2.0:2.4。最后,利用 CSDCorrections1.6 软件(Higgins, 2002a, b)进行矿物定量化结构参数计算,并根据所得参数进行 CSDs 和 SDPs 分析。

定量化结构参数主要有 CSD 曲线的截距、斜率、特征长,矿物的最大粒度(L_{max}),定向程度(*AF* 值),长宽比(*AR* 值)和空间展布形式的 *R* 值等。截距为 CSD 曲线与纵轴的交点,为晶体最终成核密度的自然对数,代表着成核速率,而斜率为晶体生长速率和生长时间乘积的负倒数,代表粒度为零的晶体到粒度无限大的所有晶体的平均粒度,可以代表生长速率(Marsh, 1988, 1998)。特征长为 CSD 曲线斜率的负倒数,和斜率具有相同的指示意义。*AF* 值可以反映出晶体的定向程度,*AF* 值越大则定向程度越好(Meurer and Boudreau, 1998),*AR* 值为晶体的长宽比。SDPs 中 *R* 值可以定量描述二维空间晶体的空间分布形式,为分析区域内所有晶体间相邻最短距离的平均值与分析晶体间最短距离的随机分布预测值的比值,受相邻晶体最短距离和晶体密度影响。

4 分析结果

4.1 CSDs

4.1.1 橄榄辉长苏长岩

斜长石具有直线型 CSD 曲线,曲线斜率变化范围为-2.23~-3.46,截距为 2.23~3.78。样品 WJS-20 和 WJS-21 中斜长石斜率与截距变化较小,在 CSD 曲线上表现出竖直向上平移的特征,WJS-13 具有最小的截距和最大的斜率,与前两个样品相比,在粒度为 1 mm 处具有逆时针旋转的变化特征,但截距最大的 WJS-21 样品斜率并非最小,不同于结构粗化的曲线特征(图 3a)。单斜辉石也具有直线型 CSD 曲线,曲线斜率变化范围为-2.54~-3.33,截距为 1.68~2.76(表 2),斜率与截距的相关性并不明显,CSD 曲线上总体表现出向上平移的特征(图 3a)。

4.1.2 辉长苏长岩

斜长石具有直线型 CSD 曲线,样品 WJS-23 和 WJS-36 分别在粒度为 0.89 mm 和 0.56 mm 处具有较弱的上凸特征,斜率总体变化范围为-1.65~-2.42,截距为 1.31~2.60(表 1),在 CSD 曲线上表现出斜率变化不大、截距逐渐增大的向上平移的特征(图 3b)。单斜辉石具有直线型 CSD 曲线,样品 WJS-23 和 WJS-30 分别在粒度为 0.51 mm 和 0.24 mm 处具有明显上凸特征。CSD 曲线斜率变化范围较小(-2.40~-4.38),而截距变化较大(1.49~3.97)(表 2),在 CSD 曲线上表现为向上平移的特征(图 3b)。

4.1.3 氧化物辉长岩

斜长石具有直线型 CSD 曲线,其中样品 WJS-6 和 WJS-24 在粒度 0.47 mm 处具有上凸的特征。CSD 曲线斜率和截距变化范围分别为-1.44~-1.88 和 0.49~1.60(表 1),显示出斜率基本一致而截距变化较大的向上平移的特征。单斜辉石具有

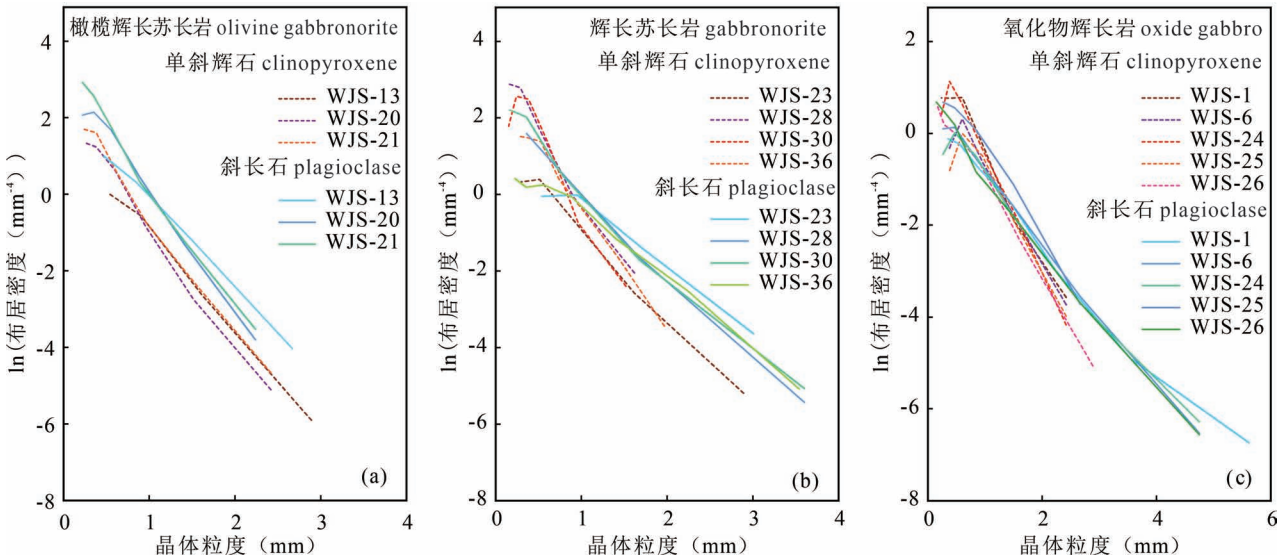

图 3 扬子地块北缘望江山岩体中部带橄榄辉长苏长岩、辉长苏长岩和氧化物辉长岩中斜长石和单斜辉石 CSD 曲线

Fig. 3 Compilation of the CSD curves of plagioclase and clinopyroxene of the olivine gabbronorite unit, gabbronorite unit and oxide gabbro unit in the MZ of the Wangjiangshan intrusion in the northern margin of the Yangtze Block

直线型 CSD 曲线,除样品 WJS-26 在小颗粒处没有上凸特征外,其余样品在粒度 0.38mm 和 0.60mm 处均出现上凸的特征。斜率和截距变化范围分别为 −2.10~−2.54 和 1.12~2.10(表 2),与斜长石一致,也表现出斜率变化较小、截距变化较大的向上平移的特征。

4.2 SDPs

橄榄辉长苏长岩中斜长石 R 值为 1.16~1.25,在 SDP 图解上与样品中除斜长石外的其他矿物总量表现为负相关关系。单斜辉石 R 值为 1.08~1.23,在 SDP 图解上与样品中除单斜辉石外的其他矿物总量也呈现出负相关关系,均与机械压实的趋势一致(图 4)。辉长苏长岩中斜长石 R 值为 1.18~1.30,在 SDP 图解上呈现出斜率较小的负相关趋势,与机械压实趋势一致。单斜辉石 R 值为 0.96~1.04,在 SDP 图解上表现为斜率较大的负相关关系,与过度生长趋势一致(图 4)。氧化物辉长岩中斜长石 R 值为 1.14~1.21,在 SDP 图解上表现为斜率较小的负相关趋势,与机械压实的趋势一致。单斜辉石 R 值为 0.99~1.15,在 SDP 图解上相关性较弱,没有明显的相关性(图 4)。

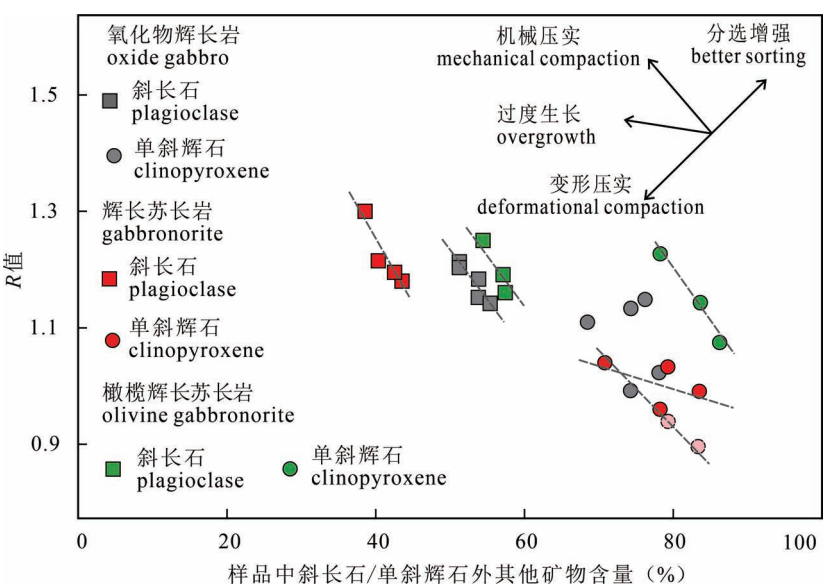

图 4 扬子地块北缘望江山岩体中部带橄榄辉长苏长岩、辉长苏长岩和氧化物辉长岩中斜长石和单斜辉石 SDP 图解(据 Jerram 等(1996))。粉红色圆圈为辉长苏长岩单斜辉石校正后的值(详见后文)

Fig. 4 Spatial distribution patterns for plagioclase and clinopyroxene of the olivine gabbronorite unit, gabbronorite unit and oxide gabbro unit in the MZ of the Wangjiangshan intrusion in the northern margin of the Yangtze Block (after Jerram et al., 1996). The pink circles represent the corrected R-values of clinopyroxene of the gabbronorite of MZb

表 1 扬子地块北缘望江山岩体中部带橄榄辉长苏长岩、辉长苏长岩和氧化物辉长岩中斜长石 CSD 和 SDP 参数

Table 1 Parameters of CSDs and SDPs for plagioclase of the olivine gabbronorite unit, gabbronorite unit and oxide gabbro unit in the MZ of the Wangjiangshan intrusion in the northern margin of the Yangtze Block

岩性	样号	颗粒数	*AR*	*AF*	圆度	测量面积(mm^2)	薄片中含量(%)	CSD 计算含量(%)	L_{max}(mm)	截距	斜率	特征长	*R* 值
氧化物辉长岩	WJS-6	353	2.24	0.04	0.5	210	48.7	47.2	6.73	0.80	−1.60	0.63	1.20
氧化物辉长岩	WJS-26	263	2.22	0.26	0.5	172	46.2	40.9	5.77	0.68	−1.62	0.62	1.15
氧化物辉长岩	WJS-1	357	2.28	0.07	0.5	228	46.1	51.9	4.81	0.49	−1.44	0.69	1.18
氧化物辉长岩	WJS-24	324	2.18	0.30	0.5	196	44.6	44.9	4.77	0.69	−1.58	0.63	1.14
氧化物辉长岩	WJS-25	360	2.16	0.67	0.5	140	48.7	46.9	3.63	1.60	−1.88	0.53	1.21
辉长苏长岩	WJS-36	400	2.16	0.71	0.5	213	57.4	49.0	3.38	1.31	−1.71	0.58	1.20
辉长苏长岩	WJS-30	346	1.89	0.37	0.6	103	59.6	54.3	4.28	2.60	−2.42	0.41	1.22
辉长苏长岩	WJS-23	578	2.00	0.29	0.6	323	61.4	55.7	3.65	1.41	−1.65	0.56	1.30
辉长苏长岩	WJS-28	320	1.92	0.14	0.6	193	56.4	49.0	3.69	2.34	−2.30	0.43	1.18
橄榄辉长苏长岩	WJS-13	381	2.27	0.53	0.5	114	45.5	47.8	3.19	2.23	−2.23	0.45	1.25
橄榄辉长苏长岩	WJS-21	440	2.12	0.19	0.6	63	42.8	39.4	2.35	3.78	−3.46	0.29	1.19
橄榄辉长苏长岩	WJS-20	373	2.02	0.15	0.6	63	42.6	38.5	2.29	3.42	−3.20	0.31	1.16

注:L_{max}:每个样品中四个最大斜长石颗粒长轴的平均值;*AF*:定向程度;*AR*:晶体长宽比;*R* 值:空间分布 *R* 值;特征长:斜率的负倒数。为保证实际矿物含量与 CSD 测量体积含量可能接近,其中 WJS-23 三轴比为 1∶2.4∶3.0;其余样品三轴比为:1∶2.7∶3.0。

表 2 扬子地块北缘望江山岩体中部带橄榄辉长苏长岩、辉长苏长岩和氧化物辉长岩中单斜辉石 CSD 和 SDP 参数

Table 2 Parameters of CSDs and SDPs for clinopyroxene of the olivine gabbronorite unit, gabbronorite unit and oxide gabbro unit in the MZ of the Wangjiangshan intrusion in the northern margin of the Yangtze Block

岩性	样号	颗粒数	*AR*	*AF*	圆度	测量面积(mm^2)	薄片中含量(%)	CSD 计算体积(%)	L_{max}(mm)	截距	斜率	特征长	*R* 值
氧化物辉长岩	WJS-6	322	1.89	0.15	0.6	122	25.7	26.7	2.85	1.46	−2.14	0.47	1.13
氧化物辉长岩	WJS-26	272	1.91	0.19	0.6	98	21.9	22.0	3.17	1.12	−2.10	0.48	1.02
氧化物辉长岩	WJS-1	381	1.74	0.07	0.5	110	31.5	33.6	2.20	2.01	−2.39	0.42	1.11
氧化物辉长岩	WJS-24	389	1.79	0.21	0.6	95	25.7	27.3	2.05	2.10	−2.54	0.39	0.99
氧化物辉长岩	WJS-25	282	1.90	0.36	0.6	108	23.7	23.7	2.57	1.41	−2.17	0.46	1.15
辉长苏长岩	WJS-36	429	1.92	0.28	0.6	76	21.7	23.5	1.78	2.80	−3.12	0.32	0.96
辉长苏长岩	WJS-30	320	1.67	0.12	0.6	33	20.7	21.0	1.51	3.97	−4.38	0.23	1.03
辉长苏长岩	WJS-23	432	2.02	0.36	0.6	115	16.4	19.6	3.39	1.49	−2.40	0.42	0.99
辉长苏长岩	WJS-28	257	1.65	0.14	0.6	32	29.1	29.1	1.68	3.68	−3.76	0.27	1.04
橄榄辉长苏长岩	WJS-13	286	1.82	0.38	0.6	85	16.3	18.1	2.30	1.68	−2.54	0.39	1.14
橄榄辉长苏长岩	WJS-21	258	1.93	0.23	0.6	48	21.7	21.0	2.25	2.76	−3.27	0.31	1.23
橄榄辉长苏长岩	WJS-20	264	1.95	0.15	0.6	39	13.7	15.8	1.96	2.58	−3.33	0.30	1.08

注:L_{max}:每个样品中四个最大单斜辉石颗粒长轴的平均值;*AF*:定向程度;*AR*:晶体长宽比;*R* 值:空间分布 *R* 值;特征长:斜率的负倒数。样品三轴比为:1∶2.0∶2.4。

表 3 扬子地块北缘望江山岩体中部带橄榄辉长苏长岩、辉长苏长岩和氧化物辉长岩中封闭粒间熔体比例和与样品平衡熔体的微量元素组成

Table 3 Estimated trace element compositions of the melt at a given fraction of trapped liquid (F_{TL}) value for the samples from the olivine gabbronorite unit, gabbronorite unit and oxide gabbro unit in the MZ of the Wangjiangshan intrusion in the northern margin of the Yangtze Block

岩性	橄榄辉长苏长岩			辉长苏长岩				氧化物辉长岩				
样号	WJS-13	WJS-20	WJS-21	WJS-23	WJS-28	WJS-30	WJS-36	WJS-1	WJS-6	WJS-24	WJS-25	WJS-26
F_{TL}	28%	29%	33%	15%	14%	14%	23%	10%	11%	10%	12%	7%
平衡熔体微量元素组成($\times10^{-6}$)												
Ti	15212	16157	20223	15138	12706	11717	16878	21191	18238	19800	20186	18553
K	28117	4529	10608	9565	6058	6855	8004	12274	13059	12389	10347	13819
P	1550	1690	2093	1631	1869	1473	2002	2451	2333	2534	2053	2214
Ba	1091	150	750	584	454	444	511	600	638	671	627	825

岩性	橄榄辉长苏长岩			辉长苏长岩				氧化物辉长岩				
Sr	403	351	419	445	427	460	436	514	606	609	604	699
Zr	175	208	267	225	151	148	234	224	208	186	191	193
Y	52.2	52.5	62.5	48.3	47.6	42.1	57.9	67.7	58.1	62.6	59.7	49.5
Ce	45.4	39.1	36.8	46.5	36.4	39.5	49.0	55.5	53.7	55.6	53.1	54.2
Nd	23.8	24.2	29.6	25.8	25.8	24.8	31.9	37.4	37.4	35.8	36.9	31.1
La	25.0	16.2	15.8	24.9	18.6	20.2	23.8	32.1	29.2	31.9	29.7	32.1
Rb	80.2	89.4	20.3	15.8	7.5	10.5	17.4	32.1	39.7	36.0	30.4	37.3
Nb	15.0	13.7	11.0	19.2	9.7	10.3	13.9	13.7	12.0	12.5	13.1	17.1
Sm	6.76	7.98	9.15	6.61	6.97	6.66	9.07	11.2	10.0	11.2	10.3	7.37
Hf	4.80	4.98	6.81	7.11	3.87	4.24	6.06	4.88	4.52	4.17	3.47	3.65
Yb	6.00	6.45	5.72	4.89	4.44	4.17	6.05	6.55	5.64	5.08	6.57	4.37
Th	1.49	1.49	1.49	2.07	0.70	1.14	1.49	1.64	2.46	2.15	2.30	2.78
Eu	2.26	2.47	2.94	2.89	1.91	1.98	2.49	2.92	2.54	2.67	2.56	2.64
Ta	0.93	1.16	0.52	1.06	0.63	0.70	1.11	1.36	0.81	0.85	0.72	1.08
Lu	0.91	0.95	0.88	0.84	0.67	0.81	0.80	0.84	0.90	0.86	0.91	0.71
U	0.41	0.41	0.41	0.59	0.17	0.32	0.41	0.43	0.71	0.55	0.61	0.64

注:“平衡熔体微量元素组成”代表样品冷凝时与之平衡的熔体成分, 为平衡分配法计算得到。

5　讨论

5.1　封闭粒间熔体比例(F_{TL})

封闭粒间熔体(trapped liquid)是指层状岩体在冷凝过程中随着堆晶矿物的生长,最终被封闭在堆晶矿物颗粒之间而没有被排出晶粥的那一部分粒间熔体(Wager et al., 1960)。晶粥中初始粒间熔体比例约 50~70%,但在完全固结的层状岩体样品中,封闭粒间熔体比例变化较大(7%~60%; Campbell, 1978; Irvine, 1980; Shirley, 1986; Philpotts et al., 1998; Jerram et al., 2003)。因此,封闭粒间熔体比例可以用来指示晶粥中粒间熔体是否被有效排出。望江山岩体中部带岩相学特征表明橄榄辉长苏长岩为中堆晶结构(图 2a),粒间相矿物含量在 20%~30%,辉长苏长岩和氧化物辉长岩为补堆晶结构(图 2b),粒间相矿物含量在 10%~20%。然而,粒间相矿物的含量只能定性对比不同岩相带粒间熔体排出的程度,不能代表封闭粒间熔体比例(F_{TL})。本次研究根据 Bédard (1994, 2001) 和 Bédard 等(2009)提出的平衡分配法(equilibrium distribution method),并结合全岩成分(王岩等, 2019)计算了封闭粒间熔体比例,详细计算方法见 Guo Feng 等(2015)和 Wang Mengxi 和 Wang Christina Yan (2020)。计算结果表明望江山岩体中部带橄榄辉长苏长岩、辉长苏长岩和氧化物辉长岩的 F_{TL} 分别为:28%~33%、14%~23%和 7%~12%,说明辉长苏长岩和氧化物辉长岩中粒间熔体被有效排出,而橄榄辉长苏长岩中粒间熔体未被有效排出。

5.2　粒间熔体的排出方式

橄榄辉长苏长岩中斜长石和单斜辉石 CSD 曲线均为直线型,而且总体表现为平行上移的特征,与机械压实的曲线特征一致(图 3a)(Higgins, 2002a)。在 SDP 图解中,斜长石和单斜辉石均为斜率较小的负相关关系(图 4),也与机械压实作用的趋势一致(Jerram et al., 1996)。因此斜长石和单斜辉石的 CSDs 和 SDPs 均表明橄榄辉长苏长岩粒间熔体的排出方式为机械压实。

辉长苏长岩中斜长石和单斜辉石均具有平行的直线型 CSD 曲线(图 3b),与机械压实的特征一致(Higgins, 2002a)。在 SDP 图解上,斜长石表现出机械压实的变化趋势(图 4),而单斜辉石表现为相关性较弱的过度生长趋势,因此单斜辉石的 CSD 曲线与 SDP 变化趋势所反映的岩浆过程不一致。样品 WJS-23 和 WJS-30 中单斜辉石的 CSD 曲线在小颗粒处具有明显的上凸特征(图 3b),说明单斜辉石小颗粒发生了丢失。这可能是在粒间熔体排出过程中,由于小颗粒单斜辉石受重力的影响最小,在机械压实作用下被粒间熔体携带一起排出晶粥所致。从 CSD 曲线特征可知,这一过程相当于减少了单斜辉石小颗粒晶体的数量,类似于增强了晶体的分选而导致 R 值增大。我们以 Jerram 等(1996)研究为基础,选择符合单斜辉石小颗粒晶体减少模型(分选指数 σI 从 0.67 减至 0.45,R 值改变量为 0.1)的 R 值改变量作为校正参数,对 WJS-23 和 WJS-30 单斜辉石 R 值进行校正。校正后辉长苏长岩所有样品在 SDP 图解上具有斜率较小的负相关关系,与机械压实的趋势一致(图 4)。因此,辉长苏长岩粒间熔

体的排出方式仍为机械压实。斜长石没有与粒间熔体一起排出可能与斜长石结晶较早有关,因为体系中斜长石结晶开始较早,特别是在斜长石成核阶段,压实作用还未发生,无法将小颗粒斜长石排出,而当压实作用程度开始之后,由于单斜辉石的结晶常常将小颗粒斜长石包裹,导致小颗粒斜长石无法排出晶粥。

氧化物辉长岩中斜长石和单斜辉石均具有一系列相互平行的 CSD 曲线(图 3c),与机械压实的曲线特征一致。在 SDP 图解中,斜长石具有与机械压实相同的趋势(图 4),而单斜辉石相关性不明显,其 CSDs 和 SDPs 所反映的岩浆过程不一致。我们认为这与辉长苏长岩中单斜辉石的情况相同,是小颗粒单斜辉石随粒间熔体排出的结果,不同的是所有氧化物辉长岩样品中单斜辉石 CSD 曲线均表现出小颗粒处的上凸特征,说明氧化物辉长岩机械压实作用效率高于辉长苏长岩,导致所有样品 R 值均发生了不同程度的改变,从而掩盖了机械压实在单斜辉石 SDP 图解中的趋势。因此,氧化物辉长岩粒间熔体的排出方式仍为机械压实作用,且效率高于辉长苏长岩。

综合 CSDs、SDPs 和 F_{TL} 等结果可知,望江山岩体中部带不同岩相带粒间熔体的排出方式均为机械压实作用,且从 MZa 中橄榄辉长苏长岩到辉长苏长岩再到 MZb 中氧化物辉长岩机械压实效率逐渐增强。

5.3 影响不同岩相带机械压实作用效率的因素

压实效率可以通过压实速率与堆晶速率相对大小进行表征(McKenzie, 1984; Tegner et al., 2009; Namur and Charlier, 2012),压实速率大于堆晶速率时压实作用才可发生,且二者差值越大压实作用越容易发生且效率越高。因此,我们对望江山岩体中部带样品的堆晶速率和压实速率进行了模拟计算。堆晶速率根据 Irvine (1970) 的方法进行计算,结果表明望江山岩体中部带橄榄辉长苏长岩、辉长苏长岩和氧化物辉长岩堆晶速率分别为 0.84~0.27 m/a、0.26~0.18 m/a 和 0.15~0.13 m/a。压实速率根据 McKenzie (1984, 1985) 和 Sparks 等(1985)的方法,假设堆晶矿物和粒间熔体达到了结构平衡,即当晶粥孔隙率很低时,孔隙没有被封闭,粒间熔体还能够与主体岩浆进行物质交换(Hunter, 1987; Mathez et al., 1997),则压实速率($\omega-W$)有以下关系:

$$\omega-W=\omega_0\left[1-\frac{1}{\cosh\dfrac{h}{\delta_c}}\right] \tag{1}$$

其中 ω 为熔体排出速度;W 为晶体沉降速度;h 为某时刻堆晶层厚度;δ_c 为堆晶层发生压实作用的理论厚度:

$$\delta_c=\sqrt{\frac{\xi+\frac{4}{3}\eta}{\mu}\cdot K_\Phi} \tag{2}$$

其中 ξ 和 η 为分别为晶粥层的体积黏度和剪切黏度,μ 为熔体黏度,K_Φ 为晶粥层的渗透率。

ω_0 为当压实没有发生而且熔体和初始孔隙率不变的情况下,晶体和熔体之间的相对速度:

$$\omega_0=\frac{K_\Phi(1-\Phi)(\rho_s-\rho_l)\mathrm{g}}{\mu\Phi} \tag{3}$$

其中 ρ_s 和 ρ_l 分别为堆晶矿物和熔体密度;g 为重力加速度;μ 为熔体黏度;Φ 为晶体孔隙率;K_Φ 为堆晶层的渗透率:

$$K_\Phi=\frac{\Phi^{5.5}a^2}{5.6} \tag{4}$$

其中 a 为晶体粒度,Φ 为晶粥层孔隙率。

为了得到准确的压实速率,我们对模拟计算过程中相关参数的选择原因如下:①晶体粒度采用样品中矿物的平均粒度;②望江山岩体与 Skaergaard 岩体具有相似的堆晶组合,晶粥层黏度选用前人对 Skaergaard 岩体计算的相应值(10^{15} Pa·s, Tegner et al., 2009; McKenzie, 2011);③橄榄辉长苏长岩和辉长苏长岩样品具有相似的平衡熔体组成,如 La、Ce、Sm、Nd、Th、U 等元素(表 3),且粒间相没有指示熔体黏度明显增大的特征矿物(如铁钛氧化物)的大量出现,其熔体黏度采用岩浆黏度值(45 Pa·s, McBirney, 1993),而氧化辉长岩样品的平衡熔体组成更加演化,如 La、Ce、Sm、Nd、Th、U 等元素含量明显增加(表 3),且有大量铁钛氧化物结晶,其熔体黏度选择铁钛氧化物饱和时的值更为准确(85 Pa·s, Namur and Charlier, 2012);④密度差为堆晶矿物和粒间熔体密度差值的平均值;⑤晶粥孔隙率是一个连续变化的值,根据前人的计算方法,将 0.6 作为初始孔隙率,并以 e(2.718)为倍数递减,分为 3 个阶段(Φ: 0.6~0.22;Φ: 0.22~0.08;Φ: 0.08~0.03)进行计算,根据不同岩相带的封闭粒间熔体比例,确定出样品所对应的孔隙率范围。

根据以上公式及相应参数(表 4),我们计算了不同岩相带的压实速率。结果表明,压实速率随着堆晶层厚度增大而增大,随着孔隙率的减小而增大(图 5)。橄榄辉长苏长岩相带厚度为 150 m,压实速率最大为 0.33 m/a,而冷凝早期堆晶速率为 0.84

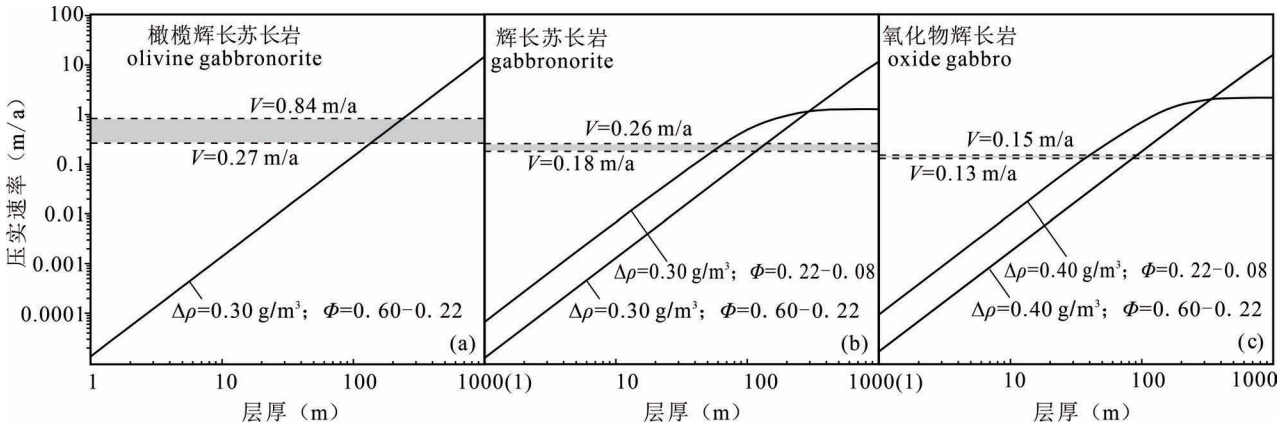

图 5 扬子地块北缘望江山岩体中部带橄榄辉长苏长岩、辉长苏长岩和氧化物辉长岩中机械压实速率与层厚关系图解

图中实线为压实速率,虚线为堆晶速率（V),Δρ 为堆晶矿物和粒间熔体密度差,Φ 为粒间熔体比例变化范围

Fig. 5 The calculated rate of compaction as a function of the thickness of the layer in olivine gabbronorite, gabbronorite and oxide gabbro in the MZ of the Wangjiangshan intrusion in the northern margin of the Yangtze Block. Solid lines represent the rate of compaction, dotted lines represent the rate of crystal accumulation (V), Δρ represents the density contrast between the cumulus crystals and the interstitial melt and Φ represents the volumetric variation of the interstitial liquid

m/a,明显大于压实速率,此时压实作用无法发生,但随着堆晶层厚度的增加,堆晶速率逐渐减小,压实速率逐渐增大,当该岩相带堆晶厚度为 135 m 时,压实速率大于堆晶速率(0.27 m/a),压实作用开始发生,因此橄榄辉长苏长岩中压实作用发生较晚,作用时间较短,导致压实效率较低(图 5a)。辉长苏长岩相带堆晶厚度为 110 m,最大压实速率为 0.54 m/a,而初始堆晶速率为 0.26 m/a,容易发生压实作用,且当该岩相带堆晶厚度为 54 m 时,压实速率大于堆晶速率(0.18 m/a),随后压实作用开始发生,因此压实作用发生较早,相对于橄榄辉长苏长岩,压实作用时间较长且效率增大(图 5b)。氧化物辉长岩相带厚度为 130 m,最大压实速率为 0.95 m/a,初始堆晶速率为 0.15 m/a,压实作用非常容易发生,且当该岩相带堆晶厚度为 38 m 时,压实速率大于堆晶速率(0.13 m/a),相比于辉长苏长岩,压实发生更早且作用时间更长、效率更高(图 5c)。因此,从橄榄辉长苏长岩到氧化物辉长岩相带,压实作用时间逐渐增长,压实效率逐渐增高。

表 4 扬子地块北缘望江山岩体中部带橄榄辉长苏长岩、辉长苏长岩和氧化物辉长岩样品计算压实速率的参数

Table 4 Parameters used to calculate the rate of compaction of samples from the olivine gabbronorite unit, gabbronorite unit and oxide gabbro unit in the MZ of the Wangjiangshan intrusion in the northern margin of the Yangtze Block

岩性	橄榄辉长苏长岩	辉长苏长岩	氧化物辉长岩
晶体粒度(mm)	1.5	2.0	3.0
晶粥层黏度(Pa·s)	10^{15}	10^{15}	10^{15}
熔体黏度(Pa·s)	45	45	85
堆晶密度(g/cm³)	2.95~3.03	2.94~3.02	3.09~3.17
熔体密度(g/cm³)	2.63~2.69	2.65~2.71	2.74~2.78
密度差(g/cm³)	0.3	0.3	0.4
孔隙率	0.6~0.22	0.22~0.08	0.22~0.08

氧化物辉长岩具有较高的堆晶矿物和粒间熔体密度差可能是其压实效率增高的主要原因(表 4),但辉长苏长岩相比于橄榄辉长苏长岩,堆晶矿物和粒间熔体密度差并没有明显增高,因此辉长苏长岩具有相对橄榄辉长苏长岩较高的压实效率可能还受其他因素控制。前人研究认为压实效率还可能与结晶过程中冷却速率的变化有关(McKenzie, 1984, 1985;Sparks et al., 1985; Tegner et al., 2009)。岩相观察显示橄榄辉长苏长岩具有辉长辉绿结构(图 2a),为快速结晶的特征,而辉长苏长岩和氧化物辉长岩为辉长结构(图 2b;图 2c),是缓慢结晶的结果,说明这 3 个岩相带的压实效率可能还与冷却速率的变化有关。因此,还需要进一步约束望江山岩体中部各岩相带的冷却速率。

岩浆冷却速率的变化可以通过 CSD 曲线的截距、特征长以及斜长石晶体形态进行判断。CSD 曲线的表达式中截距($\ln n^0$)为粒度无穷小晶体的布居密度,特征长代表所有晶体的平均粒度,分别可以用来指示晶体成核速率与生长速率,从而确定岩浆冷却速率的变化(Marsh, 1988, 1998; Higgins,

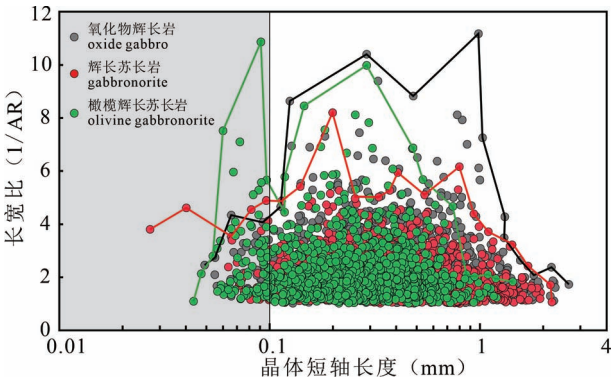

图 6 扬子地块北缘望江山岩体中部带橄榄辉长苏长岩、辉长苏长岩和氧化物辉长岩中斜长石晶体短轴长度与长宽比相关图解。阴影区域为斜长石短轴小于 0.1 mm 的区域,代表冷却速率影响的晶体范围;绿色、红色、黑色线条分别为橄榄辉长苏长岩、辉长苏长岩和氧化物辉长岩不同粒度下最大长宽比的连线

Fig. 6 The relationship of the length of short axis and aspect ratio of plagioclase crystals of the olivine gabbronorite unit, gabbronorite unit and oxide gabbro unit in the MZ of the Wangjiangshan intrusion in the northern margin of the Yangtze Block. The shadow area represents the plagioclase grains with the length of short axis less than 0.1mm, which may be affected by the rate of cooling. The green, red and black lines represent the maximum aspect ratio of plagioclase of the samples from the olivine gabbronorite unit, gabbronorite unit and oxide gabbro unit in different sizes, respectively

2006b; Higgins and Roberge, 2007)。辉长苏长岩和氧化物辉长岩中单斜辉石 CSD 曲线小颗粒处具有明显的上凸特征,截距难以准确反映其成核速率,而斜长石作为望江山岩体中部带主要堆晶矿物,其 CSD 曲线在小颗粒处上凸的特征较少,因此可以选择斜长石 CSD 曲线的截距和特征长来反映岩浆冷却速率的变化。另一方面,斜长石的晶体形态也可以反映冷却速率或过冷度的变化,斜长石短轴方向的结晶在过冷度较大的情况下会受到限制,长轴的结晶速率会得到促进,从而形成长宽比较大的斜长石(Cashman, 1992; Hammer et al., 1999; Higgins, 2006b; Holness, 2015)。但斜长石的形态常与粒度大小有关,如小颗粒斜长石具有高长宽比反映的是冷却速率较快的结晶过程,而大颗粒具有高长宽比可能是机械压实作用的结果,因为机械压实会导致晶体在垂直应力方向的晶轴生长速率增高,从而产生粒度较大且长宽比较高的斜长石(Higgins, 1991, 2006b)。因此,为了更好地判断望江山岩体中部带矿物成核过程中过冷度的变化,避免机械压实对斜长石长宽比的影响,我们选择斜长石短轴代表其粒度大小,并对不同粒度斜长石的长宽比进行统计(图 6)。

橄榄辉长苏长岩斜长石 CSD 曲线具有中部各岩相带中最大的截距(2.23~3.78)和最小的特征长(0.29~0.45),且在小颗粒(<0.1 mm)斜长石范围具有较高的长宽比(5∶1~11∶1),说明晶体的成核速率较高,生长速率较低,则结晶过程中冷却速率较快,导致堆晶速率较高,延迟了机械压实的发生,使粒间熔体没有被及时排出。相比于橄榄辉长苏长岩,辉长苏长岩斜长石 CSD 曲线截距明显减小(1.31~2.60),特征长明显增大(0.43~0.58),且小颗粒(<0.1 mm)斜长石长宽比减小(<5∶1),表明晶体成核速率的减小和生长速率的增大,岩浆冷却速率变慢,导致堆晶速率减小,使机械压实效率增高。氧化物辉长岩斜长石 CSD 曲线具有中部带最小的截距(0.49~1.60)和最大的特征长(0.53~0.69),且小颗粒(<0.1 mm)斜长石也具有较低的长宽比(<5∶1)。相比于辉长苏长岩相带,该岩相带成核速率减小,生长速率增大,暗示冷却速率进一步减小,因此堆晶速率也进一步减小,使机械压实效率增高。同时,随着铁钛氧化物大量结晶使堆晶矿物和粒间熔体的密度差增大,二者共同导致压实速率增高,使其效率达到最大,粒间熔体排出程度最高。因此,橄榄辉长苏长岩具有较低的机械压实效率是冷却速率较快和堆晶矿物与粒间熔体密度差较小共同影响的结果,辉长苏长岩机械压实效率的增大与冷却速率减小有关,而氧化物辉长岩机械压实效率达到最大值是冷却速率进一步减小以及堆晶矿物与粒间熔体密度差增大共同作用的结果。

6 结论

扬子地块北缘望江山层状岩体中部带晶粥中粒间熔体的排出方式为机械压实作用,且不同岩相带机械压实的效率不同,导致粒间熔体的排出程度也不同。MZa 中橄榄辉长苏长岩具有较高的冷却速率和较低的堆晶矿物与粒间熔体的密度差,造成较低的压实速率和较高的堆晶速率,机械压实效率较低,粒间熔体没有被有效排出;辉长苏长岩冷却速率降低使堆晶速率降低,导致机械压实效率增强,粒间熔体被有效排出。MZb 中氧化物辉长岩冷却速率的持续降低使堆晶速率进一步降低,且随着铁钛氧化物大量结晶使堆晶矿物和粒间熔体的密度差增大,

压实速率的增大使晶粥中机械压实效率达到最高,粒间熔体的排出程度也达到最高。因此,层状岩体中压实作用的效率受控于堆晶矿物和粒间熔体的密度差以及岩浆的冷却速率,较高的密度差和较低的冷却速率会提高机械压实效率,即在冷却速率较低并有铁钛氧化物结晶时机械压实作用的效率最高。

参 考 文 献 / References

(The literature whose publishing year followed by a "&" is in Chinese with English abstract; The literature whose publishing year followed by a "#" is in Chinese without English abstract)

敖文昊, 张宇昆, 张瑞英, 赵燕, 孙勇. 2014. 新元古代扬子北缘地壳增生事件: 来自汉南祖师店奥长花岗岩地球化学、锆石 LA-ICP-MS U-Pb 年代学和 Hf 同位素证据. 地质论评, 60(6): 1393~1408.

高山, 张本仁. 1990. 扬子地台北部太古宙 TTG 片麻岩的发现及其意义. 地球科学, 15(6): 675~679.

高峰. 2020. 扬子板块西北缘新元古代早-中期构造演化. 导师: 裴先治. 西安: 长安大学博士学位论文: 1~185.

耿元生, 旷红伟, 柳永清, 杜利林. 2017. 扬子地块西、北缘中元古代地层的划分与对比. 地质学报, 91(10): 2151~2174.

旷红伟, 耿元生, 柳永清, 王玉冲, 夏晓旭, 彭楠, 范正秀, 陈骁帅, 白华青. 2019. 扬子克拉通北缘"神农架群底界"的再厘定及其地层学意义. 地质学报, 93(1): 72~93.

李行, 白文吉, 陈方伦, 邹湘华, 郑新华, 杨钟堂, 陆瑶, 杨星, 胡旭峰. 1995. 扬子地块北缘和西缘前寒武纪镁铁层状杂岩及含铂性. 西安: 西北大学出版社: 1~124.

李婷. 2010. 扬子陆块北缘碑坝—西乡地区新元古代构造—岩浆作用研究. 导师: 徐学义. 西安: 长安大学硕士学位论文: 5~64.

凌文黎, 王歆华, 程建萍. 2001. 扬子北缘晋宁期望江山基性岩体的地球化学特征及其构造背景. 矿物岩石地球化学通报, 20(4): 218~221.

凌文黎, 高山, 程建萍, 江麟生, 袁洪林, 胡兆初. 2006. 扬子陆核与陆缘新元古代岩浆事件对比及其构造意义—来自黄陵和汉南侵入杂岩 ELA-ICPMS 锆石 U-Pb 同位素年代学的约束. 岩石学报, 22(2): 387~396.

刘伟, 杨晓勇, 马志鑫, 孙志明, 廖忠礼. 2018. 扬子陆块北缘上两地区二长花岗岩成因: 锆石 U-Pb 年代学、Hf 同位素及地球化学制约. 地质学报, 92(1): 65~76.

苏犁. 2004. 中国中西部几个新元古代镁铁、超镁铁岩体研究及对 Rodinia 超大陆裂解事件的制约. 导师: 周鼎武. 西安: 西北大学博士学位论文: 1~107.

王梦玺, 王焰, 赵军红. 2012. 扬子板块北缘周庵超镁铁质岩体锆石 U/Pb 年龄和 Hf—O 同位素特征: 对源区性质和 Rodinia 超大陆裂解时限的约束. 科学通报, 57(34): 3283~3294.

王岩, 王梦玺, 焦建刚. 2019. 扬子地块北缘新元古代望江山层状岩体矿物成分和铂族元素特征: 对岩浆演化过程和构造环境的制约. 地质力学学报, 25(2): 267~285.

王岩. 2019. 扬子地块北缘新元古代望江山层状岩体岩浆演化过程及成矿潜力评价. 导师: 焦建刚;王梦玺. 西安: 长安大学硕士学位论文: 26~29.

徐学义, 夏林圻, 陈隽璐, 马中平, 李向民, 夏祖春, 王洪亮. 2009. 扬子地块北缘西乡群孙家河组火山岩形成时代及元素地球化学研究. 岩石学报, 25(12): 3309~3326.

徐学义, 陈隽璐, 李向民, 马中平, 王洪亮, 夏林圻, 夏祖春, 李平. 2010. 西乡群三郎铺组和大石沟组火山岩 U-Pb 定年及岩石成因研究. 岩石学报, 26(2): 617~632.

赵凤清, 赵文平, 左义成, 李宗会, 薛克勤. 2006. 陕南汉中地区新元古代岩浆岩 U-Pb 年代学. 地质通报, 25(3): 383~388.

Ao Wenhao, Zhang Yukun, Zhang Ruiying, Zhao Yan, Sun Yong. 2014&. Neoproterozoic Crustal Accretion of the Northern Margin of Yangtze Plate: Constrains from Geochemical Characteristics, LA-ICP-MS Zircon U-Pb Chronology and Hf Isotopic Compositions of Trondhjemite from Zushidian Area, Hannan Region. Geological Review, 60(6): 1393~1408.

Bédard J H. 1994. A procedure for calculating the equilibrium distribution of trace elements among the minerals of cumulate rocks, and the concentration of trace elements in the coexisting liquids. Chemical Geology, 118 (1~4): 143~153.

Bédard J H. 2001. Parental magmas of Nain Plutonic Suite anorthosites and mafic cumulates: a trace element modeling approach. Contributions to Mineralogy and Petrology, 141: 747~771.

Bédard J H, Leclerc F, Harris L B, Goulet N. 2009. Intra-sill magmatic evolution in the Cummings Complex, Abitibi greenstone belt: tholeiitic to calc-alkaline magmatism recorded in an Archaean subvolcanic conduit system. Lithos, 111(1~2): 47~71.

Boorman S, Boudreau A, Kruger F J. 2004. The Lower Zone — Critical Zone transition of the Bushveld Complex: a quantitative textural study. Journal of Petrology, 45 (6): 1209~1235.

Campbell I H. 1978. Some problems with the cumulus theory. Lithos, 11 (4): 311~323.

Cashman K V. 1992. Groundmass crystallisation of Mount St Helens dacite 1980 ~ 1986: a tool for interpreting shallow magmatic processes. Contributions to Mineralogy and Petrology, 109 (4): 431~49.

Cashman K V, Sparks R S J, Blundy J D. 2017. Vertically extensive and unstable magmatic systems: a unified view of igneous processes. Science, 355 (6331): eaag3055.

Chen Jiangfeng, Foland K A, Xing Fengming, Xu Xiang, Zhou Taixi. 1991. Magmatism along the southeastern margin of Yangtze block: Precambrian collision of the Yangtze and Cathaysia block of China. Geology, 19 (8): 815~818.

Donev A, Cisse I, Sachs D, Variano E A, Stillinger F H, Connelly R, Torquato S, Chaikin P M. 2004. Improving the density of jammed disordered packings using ellipsoids. Science, 303: 990~993.

Gao Feng. 2020&. Early to middle Neoproterozoic tectonic evolution of the northwestern margin of the Yangtze Block: Evidence from the Hengdan Group sedimentary strata. Doctor thesis, Chang'an University, Xi'an.

Gao Shan, Zhang Benren. 1990&. The discovery of archean TTG gneisses in the northern Yangtze platform and their implications. Earth Science, 15(6): 675~679.

Gao Shan, Ling Wenli, Qiu Yumin, Lian Zhou, Hartmann G, Simon K. 1999. Contrasting geochemical and Sm-Nd isotopic compositions of Archean metasediments from the Kongling high-grade terrain of the Yangtze craton: evidence for cratonic evolution and redistribution of REE during crustal anatexis. Geochimica et Cosmochimica Acta, 63 (13~14): 2071~2088.

Garrido C J, Kelemen P B, Hirth G. 2001. Variation of cooling rate with depth in lower crust formed at an oceanic spreading ridge: Plagioclase crystal size distributions in gabbros from the Oman ophiolite. Geochemistry Geophysics Geosystems, 2 (10).

Geng Yuansheng, Kuang Hongwei, Liu yongqing, Du Lilin. 2017&.

Subdivision and Correlation of the Mesoproterozoic Stratigraphy in the Western and Northern Margins of Yangtze Block. Acta Geologica Sinica, 91(10): 2151~2174.

Guo Feng, Li Hongxia, Fan Weiming, Li Jingyan, Zhao Liang, Huang Miwei, Xu Wenliang. 2015. Early Jurassic subduction of the Paleo-Pacific Ocean in NE China: Petrologic and geochemical evidence from the Tumen mafic intrusive complex. Lithos, 224-225: 46~60.

Hammer J E, Cashman K V, Hoblitt R P, Newman S. 1999. Degassing and microlite crystallization during pre-climactic events of the 1991 eruption of Mt. Pinatubo, Philippines. Bulletin of Volcanology, 60 (5): 355~80.

Higgins M D. 1991. The origin of laminated and massive anorthosite, Sept Iles layered intrusion, Quebec, Canada. Contributions to Mineralogy and Petrology, 106(3): 340~354.

Higgins M D. 1994. Numerical modeling of crystal shapes in thin sections: estimation of crystal habit and true size. American Mineralogist, 79 (1~2): 113~119.

Higgins M D. 1996. Magma dynamics beneath Kameni volcano, Thera, Greece, as revealed by crystal size and shape measurements. Journal of Volcanology and Geothermal Research, 70(1-2): 37~48.

Higgins M D. 2002a. A crystal size-distribution study of the Kiglapait layered mafic intrusion, Labrador, Canada: evidence for textural coarsening. Contributions to mineralogy and petrology, 144(3): 314-330.

Higgins M D. 2002b. Closure in crystal size distributions (CSD), verification of CSD calculations, and the significance of CSD fans. American Mineralogist, 87 (1): 171~175.

Higgins M D. 2006a. Verification of ideal semi-logarithmic, lognormal or fractal crystal size distributions from 2D datasets. Journal of Volcanology and Geothermal Research, 154(1~2): 8~16.

Higgins M D. 2006b. Quantitative Textural Measurements in Igneous and Metamorphic Petrology. Cambridge: Cambridge University Press.

Higgins M D, Roberge J. 2007. Three magmatic components in the 1973 eruption of Eldfell volcano, Iceland: Evidence from plagioclase crystal size distribution (CSD) and geochemistry. Journal of Volcanology and Geothermal Research, 161 (3): 247~260.

Holness M B, Nielsen T F, Tegner C. 2007. Textural maturity of cumulates: a record of chamber filling, liquidus assemblage, cooling rate and large-scale convection in mafic layered intrusions. Journal of Petrology, 48 (1): 141~157.

Holness M B, Tegner C, Namur O, Pilbeam L. 2015. The earliest history of the Skaergaard magma chamber: a textural and geochemical study of the Cambridge drill core. Journal of Petrology, 56 (11): 1199~1227.

Holness M B, Vukmanovic Z, Mariani E. 2017. Assessing the role of compaction in the formation of adcumulates: a microstructural perspective. Journal of Petrology, 58 (4): 643~673.

Hunter R H, Sparks R S J. 1987. The differentiation of the Skaergaard intrusion. Contributions to Mineralogy and Petrology, 95: 451~461.

Hunter R H. 1996. Textural development in cumulate rocks. In: Cawthorn, G. A. (ed.) Layered Intrusions. Amsterdam: Elsevier, pp. 77~101.

Irvine T N. 1970. Heat transfer during solidification of layered intrusions. I. Sheets and sills. Canadian Journal of Earth Sciences, 7 (4): 1031~1061.

Irvine T N. 1980. Magmatic infiltration metasomatism, doublediffusive fractional crystallization, and adcumulus growth in the Muskox intrusion and other layered intrusions. In: Hargraves, R. B. (ed.) Physics of Magmatic Processes. Princeton, NJ: Princeton University Press, pp. 325~383.

Irvine T N. 1982. Terminology for layered intrusions. Journal of Petrology, 23 (2): 127~162.

Jerram D A, Cheadle M J, Hunter R H, Elliott M T. 1996. The spatial distribution of grains and crystals in rocks. Contributions to Mineralogy and Petrology, 125 (1): 60~74.

Jerram D A, Cheadle M J, Philpotts A R. 2003. Quantifying the building blocks of igneous rocks: are clustered crystal frameworks the foundation?. Journal of Petrology, 44 (11): 2033~2051.

Kaufmann F E, Hoffmann M C, Bachmann K, Veksler I V, Trumbull R B, Hecht L. 2019. Variations in Composition, Texture, and Platinum Group Element Mineralization in the Lower Group and Middle Group Chromitites of the Northwestern Bushveld Complex, South Africa. Economic Geology, 114 (3): 569~590.

Kuritani T, Yokoyama T, Nakamura E. 2007. Rates of thermal and chemical evolution of magmas in a cooling magma chamber: a chronological and theoretical study on basaltic and andesitic lavas from Rishiri Volcano. Journal of Petrology, 48(7): 1295~1319.

Kuang Hongwei, Geng Yuansheng, Liu Yongqing, Wang Yuchong, Xia Xiaoxu, Peng Nan, Fan Zhengxiu, Chen Xiaoshuai, Bai Huaqing. 2019&. Revision of "the bottom of Shennongjia Group" and stratigraphic implication in the northern margin of Yangtze Craton. Acta Geologica Sinica, 93(1): 72~93.

Li Hang, Bai Wenji, Cheng Fanglun, Zou Xianghua, Zheng Xinhua, Yang Zhongtang, Lu Yao, Yang Xing, Hu Xufeng. 1995&. On the mafic layered complex of pre-Cambrian and it's Pt-bearing property from northern and western edge of Yangtz massif. Xi'an: Northwest University Press, 1~124.

Li Ting. 2010&. The Study Neoproterozoic Tectonic—magmatic Events in the Northern Margin of the Yangtze Continental. Master thesis, Chang'an University, Xi'an.

Ling Wenli, Wang Xinhua, Cheng Jianping. 2001&. Geochemical Features and Its Tectonic Implication of the Jinningian Wangjiangshan Gabbros in the North Margin of Yangtze Block. Bulletin of Mineralogy, Petrology and Geochemistry, 20(4): 218~221.

Ling Wenli, Gao Shan, Cheng Jianping, Jiang Linsheng, Yuan Honglin, Hu Zhaochu. 2006&. Neoproterozoic magmatic events within the Yangtze continental interior and along its northern margin and their tectonic implication: constraint from the ELA-ICPMS U-Pb geochronology of zircons from the Huangling and Hannan complexes. Acta Petrologica Sinica, 22(2): 387~396.

Liu Wei, Yang Xiaoyong, Ma Zhixing, Sun Zhiming, Liao Zhongli. 2018&. Genesis of Monzonitic Granite in the Northern Margin of Yangtze Block: Zircon U-Pb Chronology, Hf Isotope and Geochemical Constraint. Acta Geologica Sinica, 92(1): 65~76.

Marsh B D. 1988. Crystal size distribution (CSD) in rocks and the kinetics and dynamics of crystallization. Contributions to Mineralogy and Petrology, 99 (3): 277~291.

Marsh B D. 1998. On the interpretation of crystal size distributions in magmatic systems. Journal of Petrology, 39 (4): 553~599.

Mathez E A, Hunter R H, Kinzler R. 1997. Petrologic evolution of partially molten cumulate: the Atok section of the Bushveld complex. Contributions to Mineralogy and Petrology, 129 (1): 20~34.

Meurer W P, Boudreau A E. 1998. Compaction of igneous cumulates Part I: Geochemical consequences for cumulates and liquid fractionation trends. The Journal of Geology, 106: 281~292.

McBirney A R. 1993. Igneous Petrology, 2nd edn. Boston: MA: Jones & Bartlett: 1~508.

McKenzie D. 1984. The generation and compaction of partially molten rock. Journal of petrology, 25 (3): 713~765.

McKenzie D. 1985. The extraction of magma from the crust and mantle. Earth and Planetary Science Letters 74 (1): 81~91.

McKenzie D. 2011. Compaction and crystallization in magma chambers: Towards a model of the Skaergaard intrusion. Journal of Petrology, 52(5): 905~930.

Namur O, Charlier B. 2012. Efficiency of compaction and compositional convection during mafic crystal mush solidification: the Sept Iles layered intrusion, Canada. Contributions to Mineralogy and Petrology, 163 (6): 1049~1068.

Namur O, Humphreys M C, Holness M B. 2014. Crystallization of interstitial liquid and latent heat buffering in solidifying gabbros: skaergaard Intrusion, Greenland. Journal of Petrology, (7): 1389~1427.

Namur O, Humphreys M C. 2018. Trace element constraints on the differentiation and crystal mush solidification in the Skaergaard intrusion, Greenland. Journal of Petrology, 59 (3): 387~418.

Nielsen T F D. 2004. The Shape and Volume of the Skaergaard Intrusion, Greenland: Implications for Mass Balance and Bulk Composition. Journal of Petrology, 45 (3): 507~530.

Philpotts A R, Shi J, Brutsman C. 1998. Role of plagioclase crystal chains in the differentiation of partly crystallized basaltic magma. Nature, 395: 343~346.

Rutter E H. 1983. Pressure solution in nature, theory and experiment. Journal of the Geological Society, 140 (5): 725~740.

Shirley D N. 1986. Compaction of Igneous Cumulates. The Journal of Geology, 94 (6): 795~809.

Sparks R S J, Huppert H E. 1984. Density changes during the fractional crystallization of basaltic magmas: fluid dynamic implications. Contributions to Mineralogy and Petrology, 85(3): 300~309.

Sparks R S J, Huppert H E, Kerr R C, McKenzie D P, Tait S R. 1985. Postcumulus processes in layered intrusions. Geological Magazine, 122 (5): 555~568.

Su Li. 2004&. Study of Neoproterozoic mafic and ultramafic intrusions in westerncentral China and their constraints on breakup of Rodinia Supercontinent. Doctor thesis, Northwest University, Xi'an.

Tait S R, Huppert H E, Sparks R S J. 1984. The role of compositional convection in the formation of adcumulate rocks. Lithos, 17: 139~146.

Tait S R, Jahrling K, Jaupart C. 1992. The planform of compositional convection and chimney formation in a mushy layer. Nature, 359: 406~408.

Tegner C, Thy P, Holness M B, Jakobsen J K, Lesher C E. 2009. Differentiation and compaction in the Skaergaard intrusion. Journal of Petrology, 50 (5): 813~840.

Toplis M J, Brown W L, Pupier E. 2008. Plagioclase in the Skaergaard intrusion. Part 1: Core and rim compositions in the layered series. Contributions to Mineralogy and Petrology, 155: 329~340.

Wager L R, Brown G M, Wadsworth W J. 1960. Types of igneous cumulates. Journal of Petrology, 1(1): 73~85.

Wang Mengxi, Wang Yan, Zhao Junhong. 2012&. Zircon U/Pb dating and Hf—O isotopes of the Zhouan ultramafic intrusion in the northern margin of the Yangtze Block, SW China: Constraints on the nature of mantle source and timing of the supercontinent Rodinia breakup. Chinese Science Bulletin, 57 (34): 3283~3294.

Wang Mengxi, Nebel O, Wang Christina Yan. 2016. The flaw in the crustal 'zircon archive': mixed Hf isotope signatures record progressive contamination of late-stage liquid in mafic—ultramafic layered intrusions. Journal of Petrology, 57 (1): 27~52.

Wang Mengxi, Wang Christina Yan. 2020. Crystal Size Distributions and Trace Element Compositions of the Fluorapatite from the Bijigou Fe—Ti Oxide-Bearing Layered Intrusion, Central China: Insights for the Expulsion Processes of Interstitial Liquid from Crystal Mush. Journal of Petrology, 61 (7): egaa069.

Wang Mengxi, Wang Christina Yan, Tan Wei. 2022. Compositional Evolution of Interstitial Liquid After Onset of Abundant Fe—Ti Oxide Crystallization in Crystal Mush: Insights from Late-Stage Microstructures and Mineral Compositions of the Bijigou Layered Intrusion, Central China. Journal of Petrology, 63 (4): egac025.

Wang Yan, Wang Mengxi, Jiao Jiangang. 2019&. Mineral composition and platinum-group elements of the Neoproterozoic Wangjiangshan layered intrusion at the northern margin of the Yangtze block: implications for the processes of magma evolution and tectonic setting. Journal of Geomechanics, 25(2): 267-285.

Wang Yan. 2019&. Magma evolution and Ni—Cu—(PGE) mineralization potential of the Neoproterozoic Wangjiangshan layered intrusion in the northern margin of Yangtze Block. Master thesis, Chang'an University, Xi'an.

Xu Xueyi, Xia Linqi, Cheng Junlu, Ma Zhongping, Li Xiangmin, Xia Zuchun, Wang Hongliang. 2009&. Zircon U-Pb dating and geochemical study of volcanic rocks from Sunjiahe Formation of Xixiang Group in northern margin of Yangtze Plate. Acta Petrologica Sinica, 25(12): 3309~3326.

Xu Xueyi, Chen Junlu, Li Xiangmin, Ma Zhongping, Wang Hongliang, Xia Linqi, Xia Zuchun, Li Ping. 2010&. Geochemistry and petrogenesis of volcanic rocks from Sanlangpu Formation and Dashigou Formation. Acta Petrologica Sinica, 26(2): 617~632.

Yan Danping, Zhou Meifu, Song Honglin, Wang Xinwen, Malpas J. 2003. Origin and tectonic significance of a Mesozoic multi-layer over-thrust system within the Yangtze Block (South China). Tectonophysics, 361 (3~4): 239~254.

Yao Zhuosen, Mungall J E, Jenkins M C. 2021. The Rustenburg Layered Suite formed as a stack of mush with transient magma chambers. Nature Communications, 12: 505.

Zhao Fengqing, Zhao Wenping, Zuo Yicheng, Li Zonghui, Xue Keqin. 2006&. U-Pb geochronology of Neoproterozoic magmatic rocks in Hanzhong, southern Shaanxi, China. Geological Bulletin of China, 25(3): 383~388.

Zhao Guochun, Cawood P A. 2012. Precambrian geology of China. Precambrian Research 222-223, 13~54.

Zhao Junhong, Zhou Meifu. 2009. Secular evolution of the Neoproterozoic lithospheric mantle underneath the northern margin of the Yangtze Block, South China. Lithos, 107 (3): 152~168.

Zhou Meifu, Kennedy A K, Sun Min, Malpas J, Lesher C M. 2002. Neoproterozoic arc-related mafic intrusions along the northern margin of South China: implications for the accretion of Rodinia. The Journal of Geology, 110 (5): 611~618.

The efficiency of compaction in the crystal mush of layered intrusions: Insights from crystal size distributions (CSDs) and spatial distribution patterns (SDPs) for minerals of the middle zone of the Wangjiangshan intrusion in the northern margin of the Yangtze block

LI Zhongzhou, WANG Mengxi, ZHANG Buqian, WANG Jie

School of Earth Science and Resources, Chang'an University, Xi'an, 710054

Objectives: Compaction is considered to be a common mechanism for the expulsion of interstitial liquid from the crystal mush when the abundant crystallization of Fe—Ti oxides during the mid-late stage of the solidification of layered intrusions. However, the efficiency of compaction is often different from layer to layer, and the main factors controlling the efficiency of compaction is not clear yet. The Neoproterozoic Wangjiangshan intrusion is a large and well-differentiated layered intrusion in the northern margin of the Yangtze block, and is composed of dunite, pyroxenite and troctolite in the lower zone (LZ), gabbro and gabbronorite in the middle zone (MZ) and diorite in the upper zone (UZ). The ~2000-m-thick MZ is the main part of the Wangjiangshan intrusion, and can be further divided into MZa and MZb based on the occurrence of Fe—Ti—V mineralization. Mineral composition and texture of rocks are distinct from the MZa to MZb, indicating that the different rock units in the MZ may have different mechanisms and different degrees of expulsion of interstitial liquid from the crystal mush. Therefore, we collected samples from the MZ of the Wangjiangshan intrusion and analyzed the crystal size distributions (CSDs) and spatial distribution patterns (SDPs) for clinopyroxene and plagioclase, in order to study the expulsion mechanism of interstitial liquid from crystal mush and its efficiency.

Methods: Three samples from the olivine gabbronorite unit, four samples from the gabbronorite unit of the MZb and five samples from the oxide gabbro unit of the MZb were selected for the CSD and SDP measurements for plagioclase and clinopyroxene.

Results: Plagioclase and clinopyroxene of the olivine gabbronorite unit and the gabbronorite unit of the MZb, and the oxide gabbro unit of the MZb overall show parallel CSD curves and the negative correlation in the SDP plot, suggesting that the interstitial liquid was expelled by the mechanical compaction in these three units. On the other hand, the fraction of trapped liquid (F_{TL}) of samples from the olivine gabbronorite unit, the gabbronorite unit and the oxide gabbro unit are from 28% to 33%, 14% to 23%, and 7% to 12%, respectively, calculated by the equilibrium distribution method using whole-rock composition, indicating that different degrees of mechanical compaction for these three units.

Plagioclase less than 0.1 mm of the olivine gabbronorite unit has a high aspect ratio from 5∶1 to 11∶1, and the CSD curves have intercept from 2.23 to 3.78 with the characteristic length from 0.29 to 0.45, suggesting a high rate of magma cooling. This results in a low compaction rate with a maximum of 0.33 m/a and a high rate of crystal accumulation with a minimum of 0.27 m/a of the crystal mush, leading to an inefficient mechanical compaction and a low degree of expulsion of interstitial liquid. Plagioclase less than 0.1 mm of the gabbronorite unit has a low aspect ratio (< 5∶1), and the CSD curves have intercept from 1.31 to 2.60 with the characteristic length from 0.43 to 0.58, suggesting a low rate of magma cooling. This results in a high compaction rate with a maximum of 0.54 m/a and a low rate of crystal accumulation with a minimum of 0.18 m/a of the crystal mush, leading to an efficient mechanical compaction and a slightly higher degree of expulsion of interstitial liquid. Plagioclase less than 0.1 mm of the oxide gabbro unit has a low aspect ratio (< 5∶1), and the CSD curves have intercept from 0.49 to 1.60 with the characteristic length from 0.53 to 0.69, suggesting the lowest rate of magma cooling. This results in a high compaction rate with a maximum of 0.95 m/a and a low rate of crystal accumulation with a minimum of 0.13 m/a of the crystal mush, leading to a more efficient mechanical compaction and a much

higher degree of expulsion of interstitial liquid.

Conclusions: The interstitial liquid of the three units in the MZ of the Wangjiangshan intrusion was expelled to varying degrees by the mechanical compaction. Mechanic compaction for samples from the olivine gabbronorite unit of MZa is inefficient, due to the fast magma cooling rate and the small density contrast between the cumulus and the interstitial melt. With the decrease of cooling rate, the compaction efficiency of the gabbronorite unit of MZa and oxide gabbro unit of MZb gradually increases. Simultaneously, abundant crystallization of Fe—Ti oxides may progressively increase the density contrast of the cumulus and the interstitial melt, resulting in a further increase of the compaction efficiency of the oxide gabbro unit. This study indicates that the efficiency of mechanic compaction of layered intrusions is mainly controlled by the cooling rate of magma and the density contrast of the cumulus and interstitial melt, with a distinct enhancement by the low cooling rate of magma and abundant crystallization of Fe—Ti oxides.

Keywords: Compaction; Expulsion of interstitial liquid; Crystal size distributions; Spatial distribution patterns; The Wangjiangshan layered intrusion; The northern margin of the Yangtze Block

First author: LI Zhongzhou, male, born in 1996, master student; Email: zhongzhouli@yeah.net

Corresponding author: WANG Mengxi, male, born in 1986, associate professor, mainly works on the magmatism and metallogeny; Email: mxwang@chd.edu.cn

Manuscript received on: 2022-01-31; Accepted on: 2022-06-09; Network published on: 2022-06-20

Doi: 10.16509/j.georeview.2022.06.161 **Edited by**: LIU Zhiqiang